

# Conformal Antireflective Multilayers for High-Numerical-Aperture Deep-Ultraviolet Lenses

Geon-Tae Park, Jae-Hyun Kim, Seunghun Lee, Dong In Kim, Ki-Seok An, Eungkyu Lee, Soonmin Yim,\* and Sun-Kyung Kim\*

Precise surface reflectance control at specific deep-ultraviolet (DUV) wavelengths across wide angles is crucial for semiconductor inspection and lithography tools. The inherent challenges in designing DUV antireflective multilayers stem from limited transparent materials and the resultant fabrication complexity owing to numerous interfaces. Here, wide-angle antireflective multilayers finely tuned to 248 nm designed using an active learning scheme is presented. The active learning scheme employing factorization machines (FM) identifies the optimal configurations for binary-material-based multilayers ( $\text{AlF}_3/\text{LaF}_3$ ,  $\text{AlF}_3/\text{MgF}_2$ , and  $\text{AlF}_3/\text{Al}_2\text{O}_3$ ) with varying index contrasts, achieving minimal figure-of-merit (i.e., average angular reflectance) values at predetermined total thicknesses. High-index-contrast  $\text{AlF}_3/\text{Al}_2\text{O}_3$  multilayers are fabricated via atomic layer deposition, thus enabling the conformal coating of high-numerical-aperture (NA) lenses with atomic precision. An optimized  $\text{AlF}_3/\text{Al}_2\text{O}_3$  tri-layer with a total thickness of 180 nm results in an average ( $0^\circ$ – $45^\circ$ ) reflectance of 0.4% on a  $\text{CaF}_2$  planar substrate and 0.6% on a  $\text{CaF}_2$  convex lens ( $\text{NA} = 0.47$ ), similar to the performance of an ideal single-layer coating requiring a practically unavailable refractive index. Phasor analysis, which considers only first-order reflections between adjacent layers, supports the benefits of high-index-contrast binary materials and the use of the FM-based active learning scheme in antireflective multilayer design.

## 1. Introduction

In the semiconductor industry, enhancing the resolution of inspection [1,2] and lithography [3–5] systems, as well as reducing

the transistor size to strengthen microchip integrity, are critical strategies. To achieve high performance in these systems, the use of high-numerical-aperture (NA) lenses that enable precise light focusing onto smaller areas is essential.[6,7] The effectiveness of high-NA lenses depends on the design of anti-reflective (AR) coatings that achieve near-zero surface reflectance across wide incident angles.[8,9] The necessity for AR coatings increases with the increasing complexity of optical systems, particularly in advanced processing lithography equipment used for fabricating nanoscale semiconductor chips and camera-based inspection equipment, both employing ArF (193 nm) or KrF (248 nm) lasers. This is because the total reflectance of a multi-lens system is proportional to the number of lenses used. However, the dearth of transparent materials in the deep-ultraviolet (DUV) spectrum (190–350 nm), aside from a few fluoride- and oxide-based dielectrics such as  $\text{CaF}_2$ ,  $\text{MgF}_2$ ,  $\text{LaF}_3$ ,  $\text{AlF}_3$ , and  $\text{Al}_2\text{O}_3$ , [10–13] the narrow range of refractive indices available for these dielectrics, and the need for ultrathin films with minimal interfaces to mitigate fabrication-induced stress limit the design

flexibility of DUV AR coatings. Laux et al. designed a 14-layer AR coating consisting of  $\text{MgF}_2$ ,  $\text{CaF}_2$ , and  $\text{NdF}_3$ , which achieved a near-normal ( $8^\circ$ ) transmittance of 98.8% at a wavelength of 255 nm.[14] Hamden et al. developed an 11-layer  $\text{SiO}_2/\text{Al}_2\text{O}_3$  AR coating that achieved a near-normal reflectance of 8% at a wavelength of 209 nm.[15] However, these earlier endeavors did not succeed in providing omnidirectional antireflection. Moreover, they rely on numerous interfaces that often involve more than two different materials, thus compromising economic aspects such as cost-effectiveness, fabrication tolerance, and long-term durability.

Various active-learning approaches, including memetic algorithms, adjoint methods, and genetic algorithms, have been employed to effectively explore such extensive parametric space inherent in designing multifunctional photonic devices.[16–24] To address the challenges in designing wide-angle DUV AR coatings, we implemented an active-learning strategy based on factorization machines (FM) to approximate a designed multilayer to a quadratic unconstrained binary optimization (QUBO) model by encoding it into a specific binary vector.[25,26] The strength of the FM-based active learning scheme lies in its ability to

G.-T. Park, J.-H. Kim, S.-K. Kim  
Department of Applied Physics  
Kyung Hee University  
Yongin-si, Gyeonggi-do 17104, Republic of Korea  
E-mail: [sunkim@khu.ac.kr](mailto:sunkim@khu.ac.kr)

S. Lee, D. I. Kim, K.-S. An, S. Yim  
Thin Film Materials Research Center  
Korea Research Institute of Chemical Technology  
Daejeon 34114, Republic of Korea  
E-mail: [s.yim@kriect.re.kr](mailto:s.yim@kriect.re.kr)

E. Lee  
Department of Electronic Engineering  
Kyung Hee University  
Yongin-si, Gyeonggi-do 17104, Republic of Korea

The ORCID identification number(s) for the author(s) of this article can be found under <https://doi.org/10.1002/adom.202401040>

DOI: 10.1002/adom.202401040

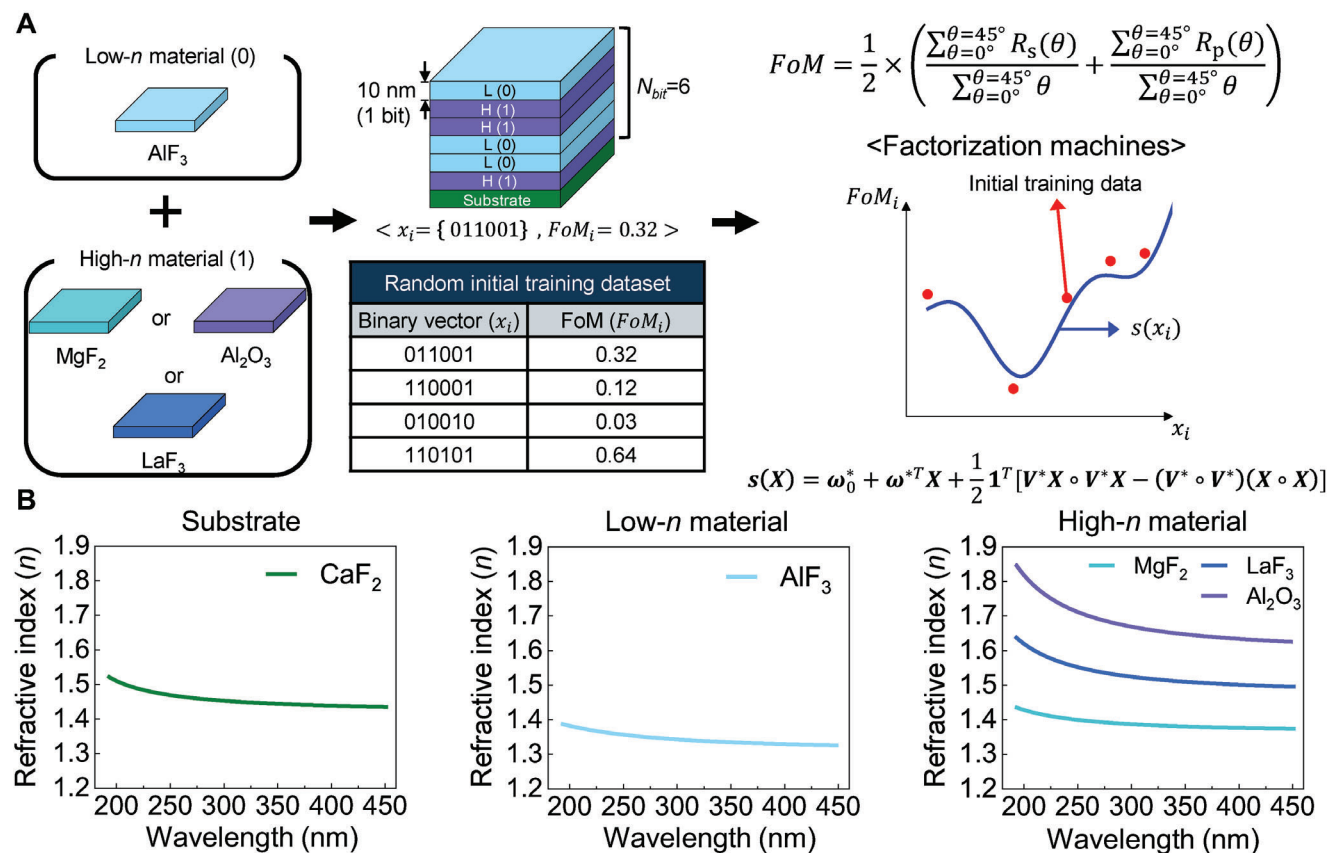


**Figure 1.** Binary-optimization-based design for AR multilayers with discrete refractive index contrasts. A) Schematics of the multilayer optimization process. The multilayers are encoded as  $N$  bits, with each bit representing a 10-nm-thick layer: '0' indicates the low- $n$  material AlF<sub>3</sub>, while '1' denotes high- $n$  materials, including MgF<sub>2</sub>, LaF<sub>3</sub>, or Al<sub>2</sub>O<sub>3</sub>. The FoM is calculated as the average angular reflectance across 0°–45° for  $s$ - and  $p$ -polarizations at a specific DUV wavelength (e.g., 248 nm). Utilizing a training dataset composed of random binary vectors  $x_i$  and their corresponding FoM values  $FoM_i$ , a surrogate function  $s(x_i)$  is formulated to mimic the FM. B) Measured refractive indices ( $n$ ) for a CaF<sub>2</sub> substrate, low- $n$  material (AlF<sub>3</sub>), and high- $n$  materials (MgF<sub>2</sub>, LaF<sub>3</sub>, and Al<sub>2</sub>O<sub>3</sub>).

discover optimal 1 or 2D photonic structures in the binary vector space at minimal computation costs, thereby achieving the targeted structured spectra. For example, Wilson et al. designed a 2D metasurface-based thermal emitter suitable for thermophotovoltaics that exhibited an absorbance spectrum fitted with the bandgap of the photovoltaics in use.<sup>[27]</sup> Kim et al. developed a SiO<sub>2</sub>/Al<sub>2</sub>O<sub>3</sub>/TiO<sub>2</sub> multilayer for energy-saving windows that selectively reflected the near-infrared band of the solar spectrum using quantum-annealing-driven binary optimization.<sup>[28]</sup>

In the current study, we employed FM-based active learning to promptly navigate the vast parametric space of AR multilayers to discover a figure-of-merit (FoM) near the global optimum.<sup>[26]</sup> This strategy enables the identification of non-intuitive (i.e., quasi-random) multilayer configurations with the capacity for wide-angle antireflection. Furthermore, it successfully addresses the material scarcity inherent to the DUV spectrum and the constraints on film thicknesses and interfaces. For fabrication, we used atomic layer deposition (ALD) for a conformal multilayer coating on the curved surfaces of high-NA lenses. The atomic-thick precision of ALD was significant in our multilayers, given the sensitivity of the AR performance to variations in individual layer thickness. Finally, we performed angular reflectance mea-

surements and energy-dispersive X-ray spectroscopy (EDS) mapping of the fabricated multilayers on both CaF<sub>2</sub> planar substrates and curved lenses. The results confirm the reliability of our design and the deposition precision. Furthermore, phasor analysis with partially reflected waves provides an intuitive perspective on the effectiveness of binary-optimization-based active learning and validates the evaluation of the wide-angle AR performance.

## 2. Result and Discussion

### 2.1. Active-Learning-Based Design

We designed DUV AR multilayers using binary materials on CaF<sub>2</sub> substrates, targeting the AR performance over a wide range of incident angles ( $\theta = 0^\circ$ – $45^\circ$ ) near the KrF laser wavelength (248 nm) (Figure 1A). The combinatorial set of binary materials comprised a low-refractive-index (low- $n$ ) material, AlF<sub>3</sub> ( $n = 1.36$ ), paired with one high-refractive-index (high- $n$ ) material, MgF<sub>2</sub> ( $n = 1.40$ ), LaF<sub>3</sub> ( $n = 1.55$ ), or Al<sub>2</sub>O<sub>3</sub> ( $n = 1.71$ ) (Figure 1B). These materials, including the CaF<sub>2</sub> substrate, were selected due to their zero-extinction coefficient ( $k$ ), avoiding parasitic absorption and enhancing transmittance in DUV applications. To implement

binary-optimization-based active learning, we assigned a binary bit to the low- $n$  material as 0 and to the high- $n$  material as 1. Each bit represents a thickness of 10 nm, which is determined heuristically to balance design resolution and computation time. Consequently, the multilayer composition can be expressed as a binary vector. For instance, the binary vector  $x_i = \{011001\}$  corresponds to a multilayer with a total thickness of 60 nm and six bits ( $N_{\text{bit}} = 6$ ), indicating, from top to bottom, 10 nm of low- $n$  material, 20 nm of high- $n$  material, 20 nm of low- $n$  material, and 10 nm of high- $n$  material. We defined the FoM as the angular ( $0^\circ$ – $45^\circ$ ) reflectance averaged for  $s$ - ( $R_s$ ) and  $p$ -polarizations ( $R_p$ ) at a specific DUV wavelength, with  $1^\circ$  increments in incident angles. The FoM values were calculated using the transfer matrix method (TMM) based on the measured refractive indices.

We employed an active learning scheme, which iteratively uses the FM as a surrogate model, to discover a binary vector that minimizes the FoM (Figure 1A). Although the TMM is not computationally expensive per multilayer, its total computational burden increases with increasing  $N_{\text{bit}}$ . This is due to the exponential increase in the number of possible configurations (i.e., algorithm complexity  $\approx 2^{N_{\text{bit}}}$ ). Therefore, we used the FM to predict the relationship between the binary vectors and corresponding FoM values, thereby saving computation time to identify an optimal binary vector. At every optimization cycle, the FM was formulated with an initial training dataset of  $m$  binary vectors of length  $N_{\text{bit}}$ , represented as a matrix  $X = \{x_1, x_2, \dots, x_m\} \in [0, 1]^{N_{\text{bit}} \times m}$  and its corresponding FoM values  $y = \{FoM_1, FoM_2, \dots, FoM_m\} \in \mathbb{R}^m$ , as follows:

$$y' = \omega_0 + \omega^T X + \frac{1}{2} 1^T [VX \circ VX - (V \circ V)(X \circ X)] \quad (1)$$

where  $\omega_0 \in \mathbb{R}$  is the global bias,  $\omega \in \mathbb{R}^{N_{\text{bit}}}$  are the linear component weight,  $1 \in [1]^m$  is the latent factor dimensionality, and  $V \in \mathbb{R}^{m \times N_{\text{bit}}}$  are the latent factors. The circle operator ( $\circ$ ) denotes the Hadamard product, which is an element-wise multiplication of two matrices of the same dimensions. The factor  $1/2$  is included to prevent the double-counting of interactions.<sup>[25]</sup> The term  $\omega^T X$  represents the linear contribution of each layer's properties (thickness and materials) to the FoM. The interaction term  $VX \circ VX - (V \circ V)(X \circ X)$  captures the pairwise interactions between two different layers. This corresponds to how each layer in the multilayer interacts with others to influence the overall AR performance. Hence, the precise modeling of these interactions enables us to design high-performance multilayers by accurately predicting how changes in one layer affect the entire system. We minimized the loss function  $L(y, y')$  with L2 regularization (Equation 2) using the stochastic gradient descent method to fit the hyperparameters ( $\omega_0, \omega, V$ ). A surrogate function  $s(X)$ , which approximates the relationship between the binary vectors and corresponding FoM values, is then formulated (Equation 3).

$$\omega_0^*, \omega^*, V^* = \arg \min L(y, y') \quad (2)$$

$$s(X) = \omega_0^* + \omega^{*T} X + \frac{1}{2} 1^T [V^* X \circ V^* X - (V^* \circ V^*)(X \circ X)] \quad (3)$$

While Equation (1) serves as a theoretical model equation for predicting the FoM of AR multilayers, Equation (3) represents a practical surrogate model to approximate these predictions during the

optimization process. Consequently, the QUBO model searches for the binary vector  $x^*$  yielding the lowest FoM using the surrogate function (Equation 4).

$$x^* = \underset{x^* \in \{0,1\}}{\operatorname{argmin}} (x^*) \quad (4)$$

After identifying the optimal binary vector  $x^*$ , TMM simulations were conducted for identical multilayers to verify two critical aspects: (i) whether the corresponding FoM was indeed the lowest value within the dataset and (ii) whether a surrogate function estimation precisely matched the actual FoM (Figure S1, Supporting Information). After the verification, the optimal binary vector and its corresponding FoM were added to the training dataset. This updated training dataset improved the surrogate function accuracy for the subsequent optimization cycle, thereby enhancing our model's prediction accuracy. While no optimization method, including the well-trained FM model, can guarantee the global minimum FoM for NP-hard (i.e., non-deterministic polynomial-time hard) combinatorial optimization problems, the FM model can identify acceptable FoM values that are at least close to the global minimum with low computational effort.<sup>[29]</sup>

## 2.2. Simulated Results and DUV AR Multilayer Analyses

Using the developed binary-optimization-based active learning, we designed DUV AR multilayers with material combinations of  $\text{AlF}_3/\text{MgF}_2$  ( $\Delta n = 0.04$ ),  $\text{AlF}_3/\text{LaF}_3$  ( $\Delta n = 0.19$ ), and  $\text{AlF}_3/\text{Al}_2\text{O}_3$  ( $\Delta n = 0.35$ ), progressively increasing  $N_{\text{bit}}$  from 11 to 20 (Figure 2A). The  $N_{\text{bit}}$  range was chosen based on the observation that the FoM values plateaued beyond  $N_{\text{bit}} = 20$ , indicating diminishing returns in the AR performance with additional increases in  $N_{\text{bit}}$ . The simulation results highlight three key insights related to AR multilayer design. First, a gradual decrease in the FoM values was observed for the  $\text{AlF}_3/\text{LaF}_3$  and  $\text{AlF}_3/\text{Al}_2\text{O}_3$  multilayers as  $N_{\text{bit}}$  increased. For example, for the  $\text{AlF}_3/\text{Al}_2\text{O}_3$  multilayers with the largest refractive-index contrast, the FoM decreased from 0.0018 at  $N_{\text{bit}} = 12$  to 0.0009 at  $N_{\text{bit}} = 18$  and finally to 0.0007 at  $N_{\text{bit}} = 20$ . Second, the  $\text{AlF}_3/\text{MgF}_2$  multilayers, characterized by both materials having lower refractive indices relative to the  $\text{CaF}_2$  substrate, exhibited only slight changes in the FoM with increasing  $N_{\text{bit}}$ , suggesting that an optimal FoM for this material combination was attainable at  $N_{\text{bit}} \leq 11$ . Third, the  $\text{AlF}_3/\text{Al}_2\text{O}_3$  multilayer exhibited the most effective AR performance across all  $N_{\text{bit}}$  values. However, we noted that a larger refractive-index contrast does not invariably enhance the AR performance, indicating that both the index contrast and absolute refractive indices are critical for determining the performance of AR multilayers (Figure S2, Supporting Information).

The bottom panel of Figure 2A illustrates the configuration of each optimized multilayer. The topmost layer was consistently identified as a low- $n$  material,  $\text{AlF}_3$ , which was chosen to suppress the initial reflectance at the interface between air and the topmost layer. As  $N_{\text{bit}}$  increases, the multilayer configuration becomes more complex although the number of physical layers does not scale linearly with  $N_{\text{bit}}$ . For instance, an  $\text{AlF}_3/\text{Al}_2\text{O}_3$  multilayer at  $N_{\text{bit}} = 18$  possesses a simple three-layer configuration. This finding underscores the importance of balancing the FoM with manufacturing simplicity, focusing on designs that

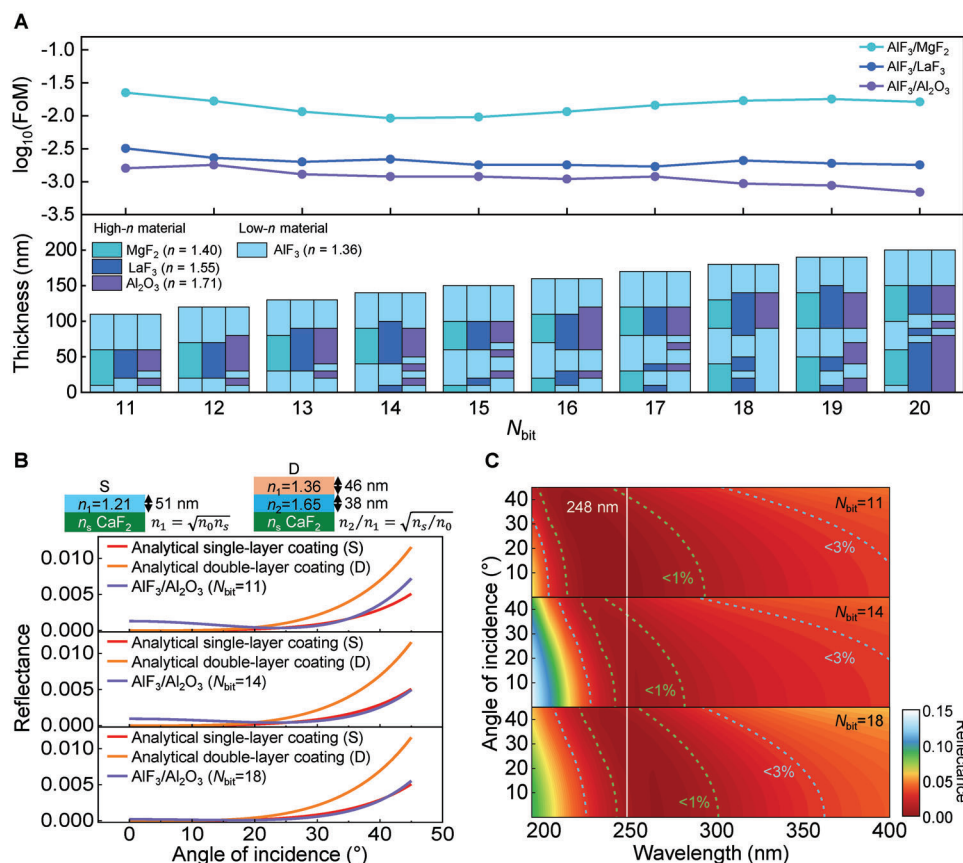


**Figure 2.** Simulated results and analyses of DUV AR multilayers with increasing  $N_{\text{bit}}$ . A) Simulated FoM values (top) and configurations (bottom) of optimized multilayers for three material pairs (AlF<sub>3</sub>/MgF<sub>2</sub>, AlF<sub>3</sub>/LaF<sub>3</sub>, and AlF<sub>3</sub>/Al<sub>2</sub>O<sub>3</sub>). B) Comparative analyses of angular reflectance among analytical single-, and double-layer coatings, and the optimized AlF<sub>3</sub>/Al<sub>2</sub>O<sub>3</sub> multilayer with varying  $N_{\text{bit}}$ . C) Simulated 2D plot of wavelength versus incident angle for the optimized AlF<sub>3</sub>/Al<sub>2</sub>O<sub>3</sub> multilayer with discrete  $N_{\text{bit}}$  values.

maintain an optimal FoM while minimizing the number of physical layers. Further simulations were conducted at an ArF laser wavelength of 193 nm to obtain the FoM values and configurations using an identical optimization process (Figure S3, Supporting Information).

The angular reflectance spectra of the AlF<sub>3</sub>/Al<sub>2</sub>O<sub>3</sub> multilayers optimized at  $N_{\text{bit}} = 11, 14$ , and  $18$  were obtained (Figure 2B). The reflectance of the optimized multilayer at  $N_{\text{bit}} = 18$  remained below 0.005 for  $\theta = 0^\circ$ – $45^\circ$ . Consistent observation of a minimum reflectance around  $\theta = 23^\circ$  (i.e., the angular range midpoint) across all configurations indicates that the developed active-learning algorithm is not solely focused on minimizing the reflectance at arbitrary incident angles, but aims to reduce the average angular reflectance within the considered range. The reflectance spectra for other material pairs, such as AlF<sub>3</sub>/MgF<sub>2</sub> and AlF<sub>3</sub>/LaF<sub>3</sub>, at  $N_{\text{bit}} = 11, 14$ , and  $18$  were also plotted as a function of  $\theta$ , revealing similar features (Figure S4, Supporting Information). In addition, the AlF<sub>3</sub>/Al<sub>2</sub>O<sub>3</sub> multilayers were compared with single- and double-layer AR coatings based on conventional design formulas using quarter-wavelength thicknesses. The analytical single-layer coating consisted of a material with  $n = 1.21$  and a thickness of 51 nm, while the analytical double-layer coating comprised materials with  $n = 1.36$  and  $1.65$  for the top and bottom layers, with thicknesses of 46 and 38 nm, re-

spectively. The simulation results revealed that each optimized AlF<sub>3</sub>/Al<sub>2</sub>O<sub>3</sub> multilayer surpassed the AR performance of the analytical double-layer coating for all considered  $N_{\text{bit}}$  values. Notably, the AlF<sub>3</sub>/Al<sub>2</sub>O<sub>3</sub> multilayer at  $N_{\text{bit}} = 18$  achieved an FoM of 0.00094, which is nearly identical to the FoM of 0.00096 obtained from the analytical single-layer coating. This achievement is particularly remarkable considering that the analytical single-layer coating requires a very low refractive index, which is practically unavailable.

We visualized the wavelength tolerance of the AlF<sub>3</sub>/Al<sub>2</sub>O<sub>3</sub> multilayers using a 2D plot of wavelength versus incident angle (Figure 2C). Within the entire range of  $\theta = 0^\circ$ – $45^\circ$ , the spectral tolerances, where the reflectance was maintained below 1%, were  $248 \pm 18$  and  $248 \pm 7$  nm at  $N_{\text{bit}} = 11$  and  $18$ , respectively. Despite the optimization criteria focusing on a single 248 nm wavelength, the optimized multilayers exhibited an appreciable spectral tolerance.

### 2.3. Phasor Analyses of the Optimized AR Multilayers

The phasor analysis, as illustrated in Figure 3A, provides a physical interpretation of the principles of multilayer coatings by considering partially reflected waves occurring at discrete



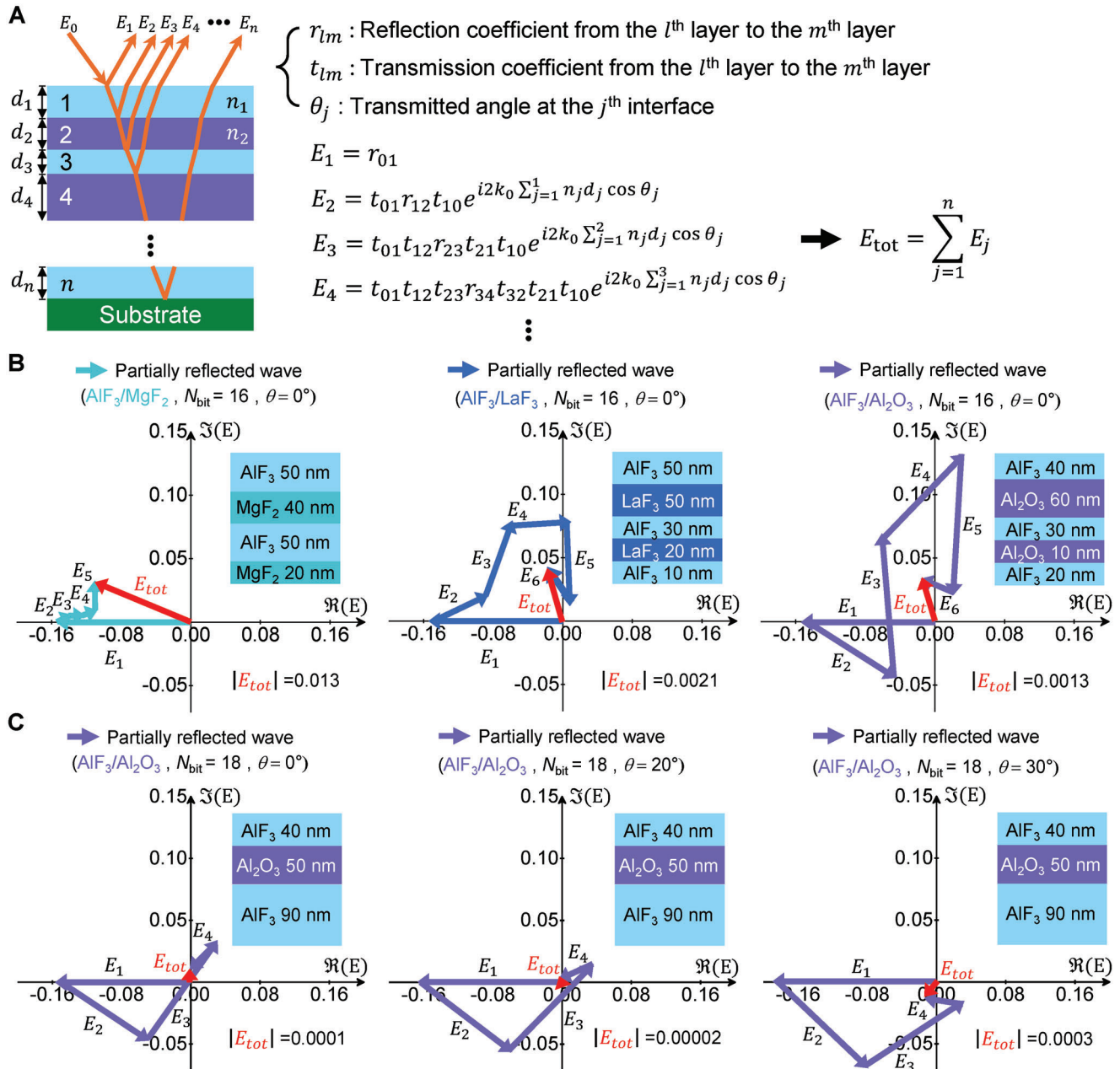


**Figure 3.** Phasor analyses for the optimized multilayers. A) Schematic describing partially reflected waves (involving a single reflection) as complex phasors. B) Phasor diagrams for multilayers with  $\text{AlF}_3/\text{MgF}_2$ ,  $\text{AlF}_3/\text{LaF}_3$ , and  $\text{AlF}_3/\text{Al}_2\text{O}_3$ , optimized at  $N_{\text{bit}} = 16$ . C) Phasor diagrams for the  $\text{AlF}_3/\text{Al}_2\text{O}_3$  multilayer optimized at  $N_{\text{bit}} = 18$  for different incident angles.

interfaces.<sup>[30–32]</sup> Initially, the complex reflection and transmission amplitudes were derived from Fresnel's coefficients, where  $r_{lm}$  and  $t_{lm}$  are the reflection and transmission coefficients between layers  $l$  and  $m$ , respectively. The phase changes were determined by the optical path differences, which depend on the transmitted angle  $\theta_j$ , layer thickness  $d_j$ , and wave vector  $k_0$ . Here,  $E_j$  refers to the phasor from a first-order reflection (involving only a single reflection) at the  $j^{\text{th}}$  interface, disregarding higher-order reflections (involving multiple reflections). The squared magnitude of the summation of all partial phasors ( $E_{\text{tot}}$ ) can be used to approximate the reflectance of a multilayer, assessing

its AR performance by examining the convergence of  $E_{\text{tot}}$  to the origin.

The phasor diagrams of the AR  $\text{AlF}_3/\text{MgF}_2$ ,  $\text{AlF}_3/\text{LaF}_3$ , and  $\text{AlF}_3/\text{Al}_2\text{O}_3$  multilayers at  $N_{\text{bit}} = 16$  and normal incidence were obtained (Figure 3B). The phasor diagram for the  $\text{AlF}_3/\text{MgF}_2$  multilayer diverged from the origin, supporting its suboptimal AR performance with a relatively high  $E_{\text{tot}}$  magnitude of 0.013. In contrast, the  $\text{AlF}_3/\text{Al}_2\text{O}_3$  multilayer achieved a significantly lower  $E_{\text{tot}}$  of 0.0013, which is an order of magnitude lower than that of the  $\text{AlF}_3/\text{MgF}_2$  multilayer, underscoring its superior AR performance. This enhancement is attributed to the larger

refractive index contrast between the binary materials, which increases the amplitude of the individual phasors and facilitates the effective convergence of  $E_{\text{tot}}$  toward the origin. If the magnitudes of individual phasors are insufficient, the total sum of the phasors will be trapped far from the origin, plateauing at  $E_1$ , the dominant phasor among others. To verify the phasor analysis accuracy, phasor diagrams for the  $\text{AlF}_3/\text{Al}_2\text{O}_3$  multilayer at off-resonance wavelengths were obtained (Figure S5, Supporting Information).

Further phasor analyses were conducted on the  $\text{AlF}_3/\text{Al}_2\text{O}_3$  multilayer ( $N_{\text{bit}} = 18$ ) at  $\theta = 0^\circ$ ,  $20^\circ$ , and  $30^\circ$  (Figure 3C). The results showed the lowest  $E_{\text{tot}}$  magnitude (0.00002) at  $\theta = 20^\circ$ , which is consistent with the angular reflectance data shown in Figure 2B, where the minimum reflectance was observed at  $\theta = 23^\circ$ . This consistency confirms the reliability of the developed active-learning-based design. Moreover, the FM model employed in this study, which addresses the interaction between two elements (e.g.,  $x_i$  and  $x_j$ ) in a binary vector, is suitable for designing AR multilayers because the phasor analysis solely considers single reflections determined by the properties (i.e., refractive index) of neighboring layers.

## 2.4. Conformal Multilayer Coating Fabrication

Conventional vacuum deposition techniques such as electron-beam evaporation, thermal evaporation, and sputtering have a relatively poor level of step coverage. These techniques are not suitable for high-NA lenses because they result in non-uniform material compositions and thicknesses due to the curved geometry of the lenses. Specifically, material compositions and their associated refractive indices can vary significantly between the center and edges of high-NA lenses, and the thicknesses become practically different. To enable precise and conformal coating of DUV AR multilayers on curved surfaces, we developed an ALD process tailored for  $\text{AlF}_3$  and  $\text{Al}_2\text{O}_3$  films. ALD is well suited for curved structures such as high-NA lenses because of its ability to provide a finely controllable film thickness, atomic-scale smoothness, and uniform deposition over complex geometries. These characteristics are especially crucial for this study, considering the oversensitivity of the AR performance to thickness variations. First, an  $\text{Al}_2\text{O}_3$  film was grown using trimethyl aluminum (TMA) as the precursor and  $\text{H}_2\text{O}$  as the reactant, with time-scale division facilitated by purge steps. To grow the  $\text{AlF}_3$  thin film, HF was used instead of  $\text{H}_2\text{O}$  as a reactant, following a previous report on the ALD of fluoride dielectrics.<sup>[33]</sup> Using a single common precursor of TMA simplifies the multilayer deposition process, achieving the largest index contrast.

Additionally, we conducted all ALD processes at a chamber temperature of  $125^\circ\text{C}$ . Despite the non-overlapping ALD growth windows of  $\text{AlF}_3$  and  $\text{Al}_2\text{O}_3$  materials, we successfully achieved a stable and reproducible film growth at  $125^\circ\text{C}$  for both. This consistency in growth temperature allowed for the monolithic deposition of multilayers. The growth per cycle of  $\text{Al}_2\text{O}_3$  and  $\text{AlF}_3$  was  $\approx 1.5$  and  $1.0 \text{ \AA}$  per cycle, respectively, highlighting precisely controllable film thicknesses that can be driven by the number of ALD cycles (Figure 4A). The incubation was negligible based on an ideal surface reaction, and the data points were linearly fitted, confirming the reproducible thickness, as determined by the number of ALD cycles.<sup>[34]</sup>

Because the ALD process relies on surface reactions with self-limiting properties, it provides uniform and predictable film thicknesses, irrespective of the structure's location and morphology. To assess conformal ALD deposition on geometries more complex than curved lens surfaces, we prepared Si nanostructures with a period of 500 nm (duty ratio of 0.5) and a depth of 600 nm (aspect ratio of 2.4). As shown in the transmission electron microscopy (TEM)/EDS images (Figure 4B), an  $\text{AlF}_3/\text{Al}_2\text{O}_3/\text{AlF}_3$  tri-layer was deposited with a consistent thickness along the surface of the Si nanostructure. The thickness variation within each constituent layer extracted from the trench, sidewall, and mesa remained below 2% of the standard deviation, establishing a uniform film thickness distribution.

We used a flow-type thermal ALD system that inherently encounters limitations in thickness uniformity owing to the chamber geometry and the flow of gases, precursors, and reactants. To assess the uniformity and identify reliable deposition regions, nine Si substrates ( $20 \times 20 \text{ mm}^2$ ) were individually positioned at the center of the ALD chamber ( $135 \times 135 \text{ mm}^2$ ) at 42.5-mm intervals (Figure 4C). This placement enabled the evaluation of the spatial uniformity throughout the chamber. As a result, for a target thickness of 40 nm for an  $\text{Al}_2\text{O}_3$  film, a high-level uniformity of  $40.2 \pm 0.16 \text{ nm}$  (0.4% standard deviation) was achieved over the entire area. For an  $\text{AlF}_3$  film with a target thickness of 35 nm, there was a slightly greater thickness variation of  $35 \pm 1.52 \text{ nm}$ , corresponding to 4.3% of the standard deviation over the same area (Figure 4D). This moderate discrepancy is believed to stem from the transport and surface reactions of HF. Nevertheless, achieving a thickness uniformity of  $<5\%$  across a wide area indicates the practicality of our ALD process for depositing films with predictable thicknesses.

In optical coating applications, surface and interfacial irregularities can significantly affect the amount of light lost through scattering. This is particularly critical in DUV applications, where strict management of surface roughness is essential.<sup>[35]</sup> Our approach, which is based on surface reactions and self-limiting behaviors, aims to generate "pinhole-free thin films"<sup>[36]</sup> that inherently address this concern. As shown in Figure 4E, we assessed the surface roughness of the  $\text{AlF}_3/\text{Al}_2\text{O}_3/\text{AlF}_3$  tri-layer using atomic force microscopy following the deposition of each layer. The root-mean-square roughness ( $R_q$ ) values for each step were 0.131 nm for a 90-nm-thick  $\text{AlF}_3$  film, 0.246 nm for a 50-nm-thick  $\text{Al}_2\text{O}_3$ , and 0.285 nm for a 40-nm-thick  $\text{AlF}_3$ . The measured surface roughness values remained below 0.2% of the total film thickness, corresponding to only a few atomic layers. This exceptional level of smoothness approaches the physical limit of the surface topology, thereby verifying the suitability of the ALD multilayer coating for DUV lenses.

## 2.5. Experimental Verification of the Designed AR Multilayers

We fabricated  $\text{AlF}_3/\text{Al}_2\text{O}_3$  multilayers optimized at  $N_{\text{bit}} = 18$  on a  $\text{CaF}_2$  substrate because of its simple three-layer configuration, and subsequently conducted reflectance measurements at normal incidence (Figure 5A). The multilayers comprised a top  $\text{AlF}_3$  layer with variable thicknesses ( $t = 40, 41$ , and  $42 \text{ nm}$ ), followed by a 50-nm middle  $\text{Al}_2\text{O}_3$  layer and a 90-nm bottom  $\text{AlF}_3$  layer. This control experiment was conducted to assess the tolerance of

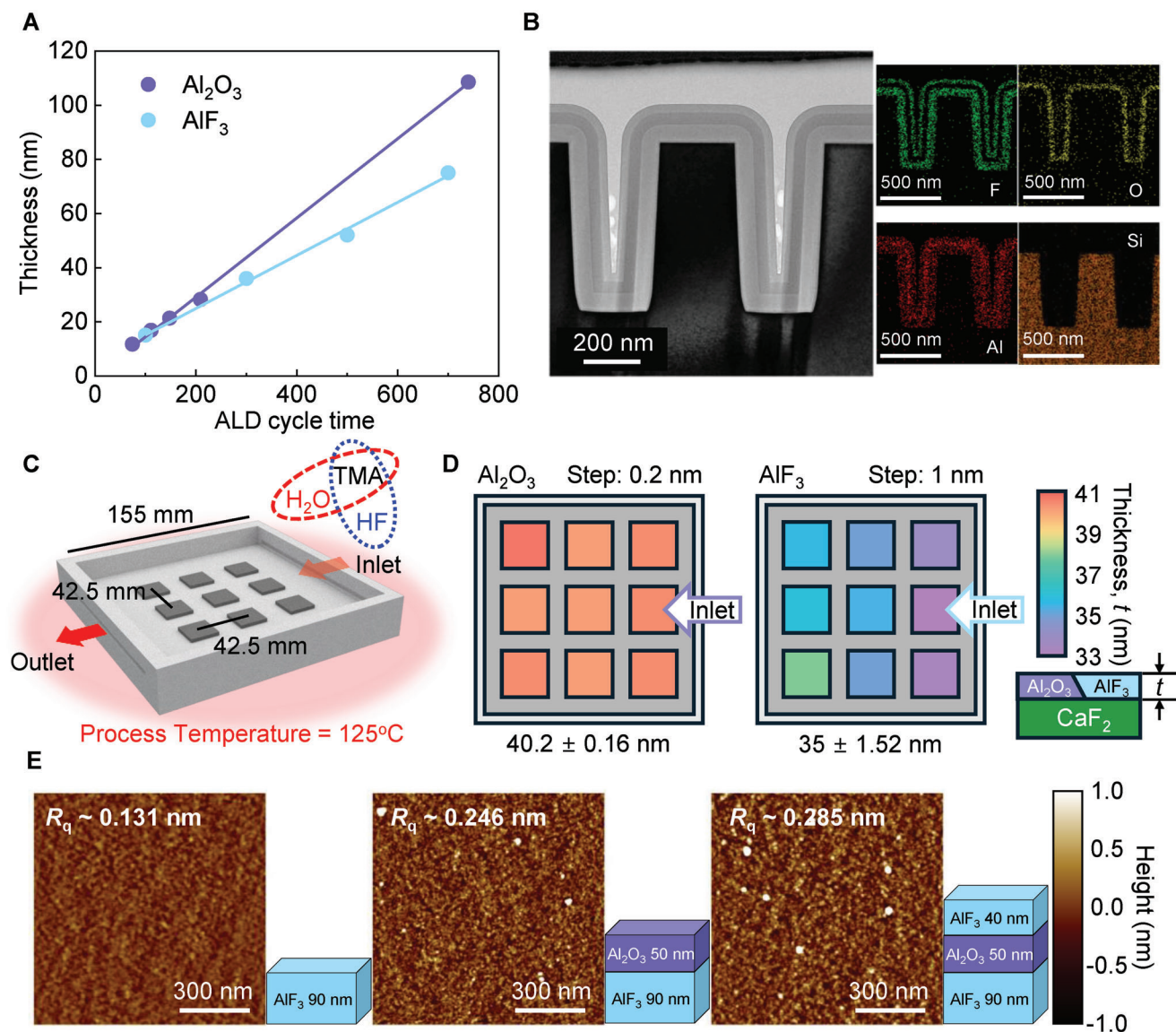


**Figure 4.** DUV AR multilayer fabrication via ALD. A) ALD growth thickness per cycle for  $\text{Al}_2\text{O}_3$  and  $\text{AlF}_3$  films. B) TEM images and EDS mapping results of an ALD-grown  $\text{AlF}_3/\text{Al}_2\text{O}_3/\text{AlF}_3$  tri-layer coating on high-aspect-ratio Si nanostructures. C) Schematic of the experiment evaluating the spatial uniformity of the ALD growth rate. D) Measured film thicknesses of  $\text{Al}_2\text{O}_3$  (left) and  $\text{AlF}_3$  (right) films at the positions marked in (C). E) Measured surface roughness of each layer comprising an ALD-grown  $\text{AlF}_3/\text{Al}_2\text{O}_3/\text{AlF}_3$  tri-layer on a  $\text{CaF}_2$  planar substrate.

the top layer thickness. As the top layer thickness increased from 40 to 42 nm, the wavelength exhibiting the minimum reflectance shifted from 252 to 266 nm. The observed minimum reflectance values ranged from 0.03% to 0.1%, which was beyond the precision of the spectrophotometer used in this study. Despite the presence of noisy signals near the minimum reflectance values, the simulation results revealed that the reflectance remained below 0.1% up to a top layer thickness of 46 nm, with the minimum reflectance wavelength extending to 280 nm (Figure S6, Supporting Information). To assess the angular dependence of AR performance, we established an experimental setup consisting of two independently rotating plates, allowing for precise angle adjustments (Figure 5B). For these measurements, we used a 266 nm laser, slightly deviating from our target wavelength of 248 nm.

The measured data exhibited a reflectance of <1% for incident angles of up to 40°, which is in good agreement with the simulated results.

For real-world applications, our study was extended to both  $\text{CaF}_2$  convex and concave lenses with conformal AR multilayer coatings (Figure 5C). Geometric parameters such as the diameter, radius of curvature, and NA are presented in Figure S7 and Table S1 (Supporting Information). The conformal multilayer coatings on the curved lenses were examined via TEM-assisted EDS mapping (Figure 5D). The mapping results verified the layer thickness precision in line with our design specifications. Reflectance measurements of identical  $\text{CaF}_2$  convex lenses, which were coated with  $\text{AlF}_3/\text{Al}_2\text{O}_3$  multilayers with a top  $\text{AlF}_3$  layer of 41 nm and others of 46 and 52 nm, exhibited a superior AR



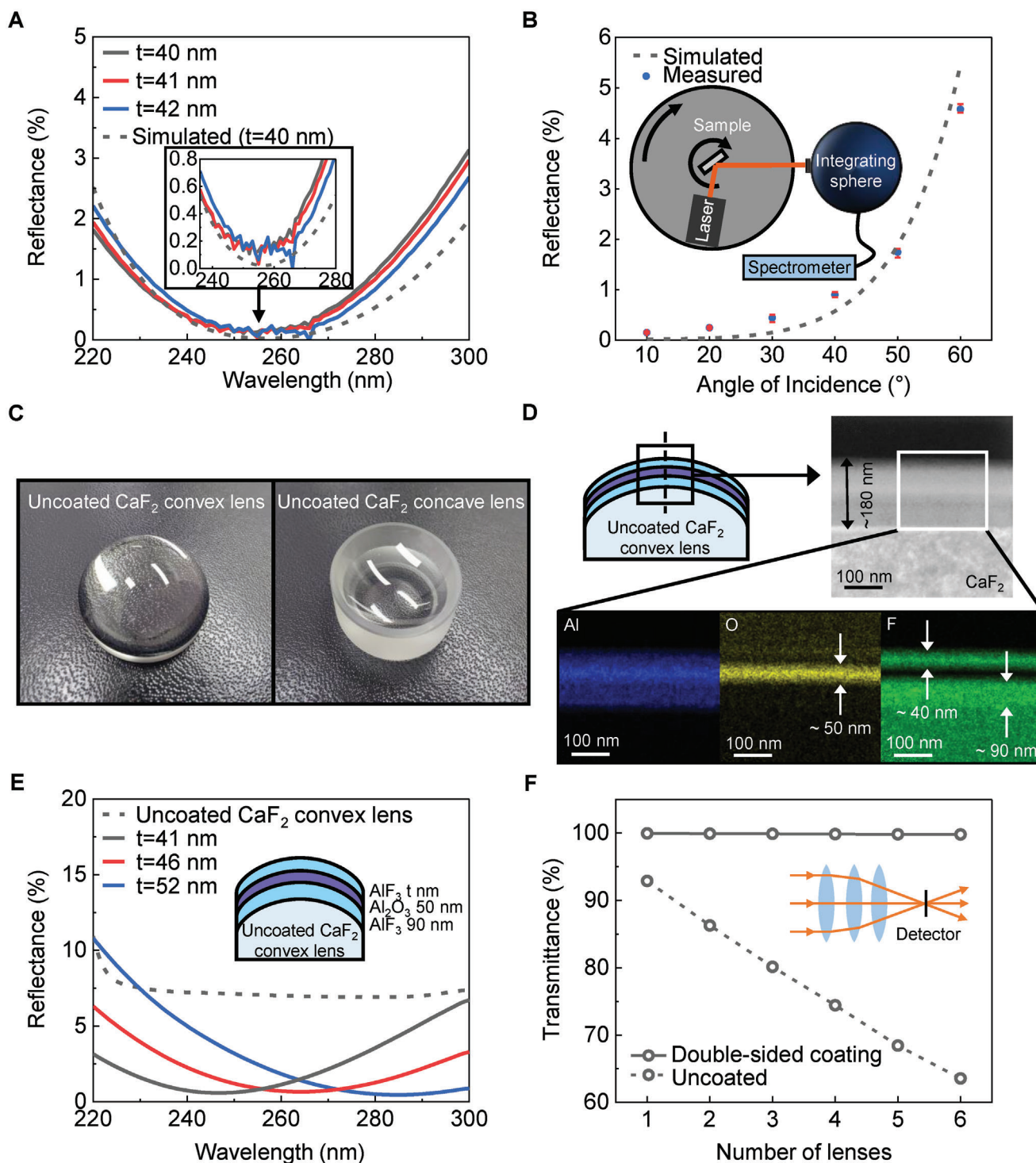


**Figure 5.** Experimental verification of the optimized AR multilayers on  $\text{CaF}_2$  substrate and lenses. A) Measured reflectance of the optimized  $\text{AlF}_3/\text{Al}_2\text{O}_3$  multilayer ( $N_{\text{bit}} = 18$ ) deposited on a  $\text{CaF}_2$  substrate, with a top layer thickness of 40, 41, and 42 nm. The inset shows the magnified results for the area indicated by the arrow. B) Measured angular reflectance of the fabricated multilayer on a  $\text{CaF}_2$  substrate with error bars. The inset shows a schematic of the experimental setup. C) Photographic images of  $\text{CaF}_2$  convex and concave lenses were used for the experiments. D) TEM/EDS imaging/mapping of the conformed  $\text{AlF}_3/\text{Al}_2\text{O}_3$  multilayer coating on the central region of a  $\text{CaF}_2$  convex lens. E) Measured reflectance results of the  $\text{AlF}_3/\text{Al}_2\text{O}_3$  multilayer coated on  $\text{CaF}_2$  convex lenses. Each multilayer has a different top  $\text{AlF}_3$  layer thickness of 41, 46, or 52 nm. F) Simulated transmittance values of a multi-lens system with and without the  $\text{AlF}_3/\text{Al}_2\text{O}_3$  multilayer coating as a function of the number of lenses. The inset shows a schematic of the simulation model.



performance compared to an uncoated lens (Figure 5E). The minimum reflectance values of the three multilayer-coated lenses were 0.6, 0.7, and 0.5%. The reflectance measurements for both the multilayer-coated  $\text{CaF}_2$  convex and concave lenses are plotted in Figure S8 (Supporting Information).

Further analysis using a ray-tracing simulation revealed the effect of increasing the number of lenses from one to six on transmittance, highlighting the importance of optimized AR coatings (Figure 5F). Without an AR coating, the total transmittance of the multi-lens system steadily decreased with an increase in the number of lenses. In contrast, lenses with double-sided coatings of the optimized  $\text{AlF}_3/\text{Al}_2\text{O}_3$  multilayers ( $N_{\text{bit}} = 18$ ) maintained a high transmittance of 99.8% regardless of the number of lenses. These findings underscore the enhanced performance of the optimized AR multilayers in complex DUV optical systems that incorporate multiple lenses.

### 3. Conclusion

We developed conformal AR multilayers for high-NA DUV lenses. Through an active-learning-based design, we identified an optimized  $\text{AlF}_3/\text{Al}_2\text{O}_3/\text{AlF}_3$  configuration with a total thickness of 180 nm, exhibiting an average angular ( $0^\circ$ – $45^\circ$ ) reflectance of 0.00094 at 248 nm. An ALD process was developed to deposit the designed  $\text{AlF}_3/\text{Al}_2\text{O}_3$  multilayers, featuring precise thickness control in conformal coatings with complex geometries. We fabricated an optimized multilayer on  $\text{CaF}_2$  planar substrates and curved lenses to validate its wide-angle AR performance. The multilayer-coated  $\text{CaF}_2$  substrates retained a reflectance of <1% for incident angles of up to  $40^\circ$ . More importantly, the conformal multilayer coating on  $\text{CaF}_2$  lenses yielded a reflectance of 0.6%.

Although this study utilized a second-order FM that accounts for the coupling between two individual layers in multilayer configurations, subsequent research can benefit from incorporating a higher-order FM. We postulate that such advancements will enable the investigation of more complex systems in which many-body interactions significantly influence optical performance. Furthermore, the FoM defined in this study, which primarily focuses on minimizing the average angular reflectance, can be expanded to consider the number of physical layers in multilayer configurations. This adjustment aims to balance optical performance with practical aspects such as economic and fabrication feasibility. Additionally, to account for the non-uniform energy distribution of incident light, such as that from a Gaussian beam, we can refine the FoM by applying an appropriate weighting factor to the incident angles. This adjustment allows for a more accurate representation of practical scenarios. Finally, the active-learning approach is not only confined to the DUV spectrum, but is broadly applicable, encompassing multi-band multilayers and microwave metasurfaces. This versatility underlines the potential for advancing photonics through efficient design strategies for photonic systems that can be transformed into binary vectors.

### 4. Experimental Section

**Active-Learning Optimization:** To optimize the AR multilayer structures, the xLearn open-source package was utilized that specializes in FM models. The methodology begins with the preparation of initial training datasets using the TMM. This dataset comprised 25 randomly generated

binary vectors for a given  $N_{\text{bit}}$  along with their corresponding FoM values. The optimization process was driven by the FM model, which was developed by learning a set of hyperparameters ( $\omega_0$ ,  $\omega$ , and  $V$ ) from the training data. This learning process was conducted through stochastic gradient descent, with a learning rate of 0.001, a regularization of 0.001, and 1000 epochs. The dimensionality of latent factor  $m$  in  $1 \in [1]^m$  was fixed at 8.

**Optical Calculation:** The TMM coded in MATLAB was utilized to evaluate the spectral properties of the optical structure. Using the TMM codes, spectra were obtained for both transmittance and reflectance across incident angles of  $0^\circ$ – $45^\circ$  and wavelengths of 180–400 nm. The NA and radius of curvature for the  $\text{CaF}_2$  convex and concave lenses were set at 0.47 and 16.7, respectively. These parameters were integrated into the surface properties of the  $\text{CaF}_2$  lens in a ray-tracing simulation (LightTools) designed for a high-NA multi-lens system. To effectively assess the beam trajectory and transmittance, 100 000 parallel rays were projected onto the lens.

**AR Multilayer Coating Fabrication:** All AR multilayer coatings were deposited using a traveling-wave-type thermal atomic-layer-deposition (ALD) reactor system (mini-ALD, NEXUSBE, Korea). Trimethyl aluminum (TMA) and HF-pyridine ( $\approx 70\%$  HF) were sourced from UPChem (Korea) and Sigma Aldrich Inc., respectively, and were used without further purification.

The growth of the  $\text{Al}_2\text{O}_3$  and  $\text{AlF}_3$  thin films was facilitated by the introduction of TMA- $\text{H}_2\text{O}$  and TMA-HF, respectively, divided by sufficient time duration of Ar purges. The TMA,  $\text{H}_2\text{O}$ , and HF-pyridine canisters were maintained at ambient temperature ( $25^\circ\text{C}$ ), while the feeding lines were heated to  $110^\circ\text{C}$  to mitigate line condensation. The working pressure for both processes was adjusted within the range of 0.3–1.0 Torr, with substrate temperatures set constantly at  $125^\circ\text{C}$  for alternating deposition procedures. The deposition sequence for  $\text{Al}_2\text{O}_3$  comprised TMA feed (0.5 s) – Ar purge (10 s) –  $\text{H}_2\text{O}$  feed (1.0 s) – Ar purge (15 s), while for  $\text{AlF}_3$ , it involved TMA feed (1.0 s) – Ar purge (30 s) – HF feed (0.7–1.5 s) – Ar purge (30 s). High-purity Ar (99.99%) was continuously supplied at a rate of 100 sccm for both feeding and purging of the precursors/reactants.

**Optical Characterization:** The reflectance measurements of the planar AR multilayer coating samples at near-normal incidence ( $7^\circ$ ) were performed using a Cary 5000 spectrophotometer (Varian) equipped with a VW Absolute Specular Reflectance Accessory (Varian). The angular reflectance was assessed using a customized rotation stage (RBB450A/M, Thorlabs) consisting of two concentric disks that rotate independently. The sample was positioned at the center of the inner disk, and a DUV laser with a 266 nm wavelength (MPL-F-266, Eforce Lasers) was installed on the outer disk. By setting the rotation ratio of the disks to 1:2, the incident angle of the laser was precisely adjusted to ensure that the path of the reflected light was correctly aligned toward the detector. The reflectance was measured using a Maya 2000 Pro spectrometer (Ocean Optics) connected to an integrating sphere (CSRM-RTC-060-SL, Labsphere), with the incident angle ( $\theta$ ) varying from  $10^\circ$ – $60^\circ$  in  $10^\circ$  increments. The reflectance of the AR multilayer coated samples was determined by normalizing the measurements against the reflected light from direct incidence without the samples. The reflectance of the AR multilayer-coated lenses was measured using a UV-3600 PLUS spectrophotometer (Shimadzu) equipped with an MPC-603 accessory.

### Supporting Information

Supporting Information is available from the Wiley Online Library or from the author.

### Acknowledgements

G.-T.P. and J.-H.K. contributed equally to this work. This work was supported by the National Research Foundation of Korea through the Basic Science Research Program (RS-2023-00207966) and the Nano Material Technology Development Program (2021M3H4A3A01055854).

## Conflict of Interest

The authors declare no conflict of interest.

## Data Availability Statement

The data that support the findings of this study are available on request from the corresponding author. The data are not publicly available due to privacy or ethical restrictions.

## Keywords

active learning, antireflective multilayer, atomic layer deposition, high index contrast, ultraviolet lens

Received: April 17, 2024  
Revised: June 3, 2024  
Published online: June 25, 2024

- [1] N. G. Orji, M. Badaroglu, B. M. Barnes, C. Beitia, B. D. Bunday, U. Celano, R. J. Kline, M. Neisser, Y. Obeng, A. Vladar, *Nat. Electron.* **2018**, 1, 532.
- [2] J. Zhang, Y. Kim, Y. Kim, R. Valencia, T. D. Milster, D. Dozer, *Jpn. J. Appl. Phys.* **2009**, 48, 03A043.
- [3] M. Rothschild, *OPN*. **2010**, 21, 26.
- [4] T. Ito, S. Okazaki, *Nature*. **2000**, 406, 1027.
- [5] S. Sreenivasan, *Microsyst. Nanoengineering*. **2017**, 3, 17075.
- [6] C. Middleton, 5 things you should know about High NA EUV lithography, <https://www.asml.com/en/news/stories/2024/5-things-high-na-euv>, (accessed: May 2024).
- [7] C. Zahlten, P. Gräupner, J. van Schoot, P. Kürz, J. Stoeldraijer, W. Kaiser, presented at EMLC. *High-NA EUV Lithography: Pushing the Limits*, Dresden, Germany, October, **2019**.
- [8] J. Jin, C. Jin, C. Li, W. Deng, Y. Chang, *JOSA. A*. **2013**, 30, 1768.
- [9] K. Pfeiffer, L. Ghazaryan, U. Schulz, A. Szeghalmi, *ACS Appl. Mater. Interfaces*. **2019**, 11, 21887.
- [10] C. Xue, K. Yi, C. Wei, J. Shao, Z. Fan, *Chin. Opt. Lett.* **2009**, 7, 449.
- [11] D. Ristau, S. Günster, S. Bosch, A. Duparre, E. Masetti, J. Ferre-Borrull, G. Kiriakidis, F. Peiro, E. Quesnel, A. Tikhonravov, *Appl. Opt.* **2002**, 41, 3196.
- [12] D. Ehrt, *Adv. Opt. Techn.* **2018**, 7, 225.
- [13] R. D. Shannon, R. C. Shannon, O. Medenbach, R. X. Fischer, *J. Phys. Chem. Ref. Data*. **2002**, 31, 931.
- [14] S. Laux, K. Mann, B. Granitz, U. Kaiser, W. Richter, *Appl. Opt.* **1996**, 35, 6216.
- [15] E. T. Hamden, A. D. Jewell, C. A. Shapiro, S. R. Cheng, T. M. Goodsall, J. Hennessy, M. Hoenk, T. Jones, S. Gordon, H. R. Ong, *JATIS*. **2016**, 2, 036003.
- [16] H. Chen, H. Jia, T. Wang, J. Yang, *J. Lightwave Technol.* **2021**, 39, 2407.
- [17] Y. Shi, W. Li, A. Raman, S. Fan, *ACS Photonics*. **2017**, 5, 684.
- [18] S. Molesky, Z. Lin, A. Y. Piggott, W. Jin, J. Vucković, A. W. Rodriguez, *Nat. Photonics*. **2018**, 12, 659.
- [19] K. Wang, X. Ren, W. Chang, L. Lu, D. Liu, M. Zhang, *Photonics Res.* **2020**, 8, 528.
- [20] Z. Li, Z. Zhou, C. Qiu, Y. Chen, B. Liang, Y. Wang, L. Liang, Y. Lei, Y. Song, P. Jia, *Adv. Opt. Mater.* **2024**, 12, 2301337.
- [21] S. Kim, W. Shang, S. Moon, T. Pastega, E. Lee, T. Luo, *ACS Energy Lett.* **2022**, 7, 4134.
- [22] Z. Liu, D. Zhu, L. Raju, W. Cai, *Adv. Sci.* **2021**, 8, 2002923.
- [23] H. Wang, Z. Zheng, C. Ji, L. J. Guo, *Mach. Learn.: Sci. Technol.* **2021**, 2, 025013.
- [24] Z. A. Kudyshev, A. V. Kildishev, V. M. Shalaev, A. Boltasseva, *Appl. Phys. Rev.* **2020**, 7, 021407.
- [25] S. Rendle, presented at *IEEE. Factorization Machines*, Sydney, Australia, December, **2010**.
- [26] J.-H. Kim, D. I. Kim, S. S. Lee, K.-S. An, S. Yim, E. Lee, S.-K. Kim, *Nanophotonics* **2023**, 12, 1913.
- [27] B. A. Wilson, Z. A. Kudyshev, A. V. Kildishev, S. Kais, V. M. Shalaev, A. Boltasseva, *Appl. Phys. Rev.* **2021**, 8, 041418.
- [28] S. Kim, S. Jung, A. Bobbitt, E. Lee, T. Luo, *Cell Rep.* **2024**, 5, 101847.
- [29] S. Kim, S.-J. Park, S. Moon, Q. Zhang, S. Hwang, S.-K. Kim, T. Luo, E. Lee, *Nano Converg.* **2024**, 11, 16.
- [30] J. Hannon, N. Hung, G. Trammell, E. Gerdau, M. Mueller, R. Rüffer, H. Winkler, *Phys. Rev. B*. **1985**, 32, 5081.
- [31] M. A. Kats, D. Sharma, J. Lin, P. Genevet, R. Blanchard, Z. Yang, M. M. Qazilbash, D. Basov, S. Ramanathan, F. Capasso, *Appl. Phys. Lett.* **2012**, 101, 221101.
- [32] X.-L. Zhang, J.-F. Song, X.-B. Li, J. Feng, H.-B. Sun, *Appl. Phys. Lett.* **2013**, 102, 103901.
- [33] Y. Lee, H. Sun, M. J. Young, S. M. George, *Chem. Mater.* **2016**, 28, 2022.
- [34] Y. Lee, J. W. DuMont, A. S. Cavanagh, S. M. George, *J. Phys. Chem. C* **2015**, 119, 14185.
- [35] H. E. Bennett, J. Porteus, *JOSA*. **1961**, 51, 123.
- [36] A. S. Yersak, Y.-C. Lee, *J. Vac. Sci.* **2016**, 34, 01A149.